PERGAMON

International Journal of Heat and Mass Transfer 44 (2001) 2261–2275

International Journal of HEAT and MASS TRANSFER

www.elsevier.com/locate/ijhmt

Thermal and flow analysis of a heated electronic component

R.-J. Yang *, L.-M. Fu

Department of Engineering Science, National Cheng Kung University, Tainan, 70101 Taiwan, ROC

Received 29 October 1999; received in revised form 1 August 2000

Abstract

This work presents the application of a newly developed numerical method to study the flow past a heated electronic component. The vortex shedding mechanism is described with the aid of a large-scale flow structure. The flow structure is also presented by streakline distributions. The computed pressure and heat flux distributions along the surface of the electronic component are discussed. Their relations with the vortex shedding are also presented.

1. Introduction

With the fast advancement of technology, the trend of electronic packaging tends to minimize component size with high performance. To achieve this goal, high dense integrated circuits (ICs) are required. It is known that the high dense ICs may generate high temperatures during their operation. Therefore, it is required to dissipate the excess heat generated in the ICs to make it work efficiently.

Generally four main methods are used to solve the thermal dissipation problem of electrical components. The first method uses a special package material with high thermal conductivity to enhance heat conduction. The second method involves attaching a fin on to the electrical component to enhance heat conduction. The third method uses a fan to cool the surface of the component. And finally, the fourth method engages a cooling water channel to lower the temperature. Of the four methods, the forced convection by a fan proves to be the most economical and efficient method. This work presents the fluid and thermal analysis of the heated electrical component via a numerical solution of the Navier–Stokes equations for the forced convection by a fan.

The artificial-compressibility method was first introduced by Chorin [1]. This method added an artificial time derivative of the pressure term, $\beta(\partial p/\partial t)$, to the incompressible continuity equation, where β is an artificial-compressibility parameter. The method was widely applied to solve incompressible flow problems such as Kwak et al. [2], Chang et al. [3], Soh [4], Ramshaw et al. [5], Yang [6], and Roger et al. [7]. These works used the artificial-compressibility method to obtain steady-state solutions, since during the iteration process there is no physical meaning. Later, Roger et al. [8], Soh et al. [9], and Yang et al. [10] used dual-time steps concept to improve the artificial-compressibility method to obtain transient-accurate solution. We will present the formulation in Section 2.

For the flow over a heated electrical component (modeled as a rectangular cylinder in the present study), the flow may have periodic vortex shedding as the Reynolds number exceeds a critical value. Therefore, a time-accurate numerical scheme is required to simulate the flow. For the cold flow over a rectangular cylinder without heat transfer, Davis et al. [11,12] and Fromm et al. [13] presented some numerical solutions. Azar et al. [14] carried out experiments and used many array sets to observe this flow field. With regard to the thermal field, Zebib et al. [15] used the finite volume method to solve the energy equation and to study the effect of various heat convection coefficients on the heat transfer. Kim et al. [16] explored the solution of thermal dissipation of three electrical components under the mixed-convection flow field.

The paper is organized as follows. In Section 2, we use the pseudo-time method to generate numerical

* Corresponding author. Tel.: +886-6-275-7575; fax: +886-6-276-6549.

E-mail address: rjyang@mail.ncku.edu.tw (R.-J. Yang).

0017-9310/01/$ - see front matter
PII: S0017-9310(00)00265-9

Nomenclature

B	width of electronic component
C_D	drag coefficient
C_p	pressure coefficient
D	drag force
f	vortex shedding frequency
g	gravitational acceleration
Gr	Grashof number
h	heat transfer coefficient
k	thermal conductivity
L	channel length
Nu	Nusselt number
p	pressure
$\overline{P}$	pseudo-time pressure
Pr	Prandtl number
$\boldsymbol{q}$	velocity vector
Re	Reynolds number
Ri	Richardson number
St	Strouhal number
T	temperature
t	time
U	velocity
u	velocity component along x-direction
u'	fluctuational velocity
v	velocity component along y-direction
$\bar{U}, \bar{V}$	velocity component in pseudo-time
W	channel height
x, y	dimensionless coordinates in the physical domain

Greek symbols

α	thermal diffusivity
β	artificial compressibility
τ	pseudo-time
v	kinematic viscosity
ρ	density

Subscripts

exit	outflow
h	pseudo-time index
in	inflow
n	physical-time index
w	wall condition
∞	free-stream condition

solutions to the unsteady incompressible Navier–Stokes equations. The numerical method produces a system of coupled non-linear algebraic equations for the pressure and fluid velocity at the advanced time level. In Section 3, some benchmark cases are tested and the computational results are discussed, which provide information about the accuracy of the developed computer program. Subsequently, the method is applied to study the thermal and flow field of a heated electronic component. The large-scale unsteady flow structure, streakline distribution and the thermal redistribution through the vortex shedding are also discussed. Finally, a few concluding remarks are given in Section 4.

2. Numerical method

The dimensionless Navier–Stokes equations for 2D incompressible flows can be written in conservative form as:

$$\frac{\partial u}{\partial x}+\frac{\partial v}{\partial y}=0, \tag{1}$$

$$\frac{\partial u}{\partial t}+\frac{\partial}{\partial x}\left(u^2+p\right)+\frac{\partial}{\partial y}(uv)=\frac{1}{Re}\left(\frac{\partial^2 u}{\partial x^2}+\frac{\partial^2 u}{\partial y^2}\right), \tag{2}$$

$$\frac{\partial v}{\partial t}+\frac{\partial}{\partial x}(uv)+\frac{\partial}{\partial y}(v^2+p)=\frac{1}{Re}\left(\frac{\partial^2 v}{\partial x^2}+\frac{\partial^2 v}{\partial y^2}\right), \tag{3}$$

where t is time, u and v the velocity components along x and y coordinates, p the pressure, Re is the Reynolds number.

We first use the Crank–Nicolson scheme to discretize Eqs. (2) and (3) as

$$\begin{aligned}\frac{u^{n+1}-u^n}{\Delta t}+\frac{1}{2}\Bigg\{&\frac{\partial}{\partial x}(u^2+p)^{n+1}+\frac{\partial}{\partial y}(uv)^{n+1}\\&-\frac{1}{Re}\left(\frac{\partial^2 u}{\partial x^2}+\frac{\partial^2 u}{\partial y^2}\right)^{n+1}+\frac{\partial}{\partial x}(u^2+p)^n+\frac{\partial}{\partial y}(uv)^n\\&-\frac{1}{Re}\left(\frac{\partial^2 u}{\partial x^2}+\frac{\partial^2 u}{\partial y^2}\right)^{n}\Bigg\}=0,\end{aligned} \tag{4}$$

$$\begin{aligned}\frac{v^{n+1}-v^n}{\Delta t}+\frac{1}{2}\Bigg\{&\frac{\partial}{\partial x}(uv)^{n+1}+\frac{\partial}{\partial y}(v^2+p)^{n+1}\\&-\frac{1}{Re}\left(\frac{\partial^2 v}{\partial x^2}+\frac{\partial^2 v}{\partial y^2}\right)^{n+1}+\frac{\partial}{\partial x}(uv)^n+\frac{\partial}{\partial y}(v^2+p)^n\\&-\frac{1}{Re}\left(\frac{\partial^2 v}{\partial x^2}+\frac{\partial^2 v}{\partial y^2}\right)^{n}\Bigg\}=0.\end{aligned} \tag{5}$$

In order to acquire the Delta form, we put $\overline{U}=\Delta u^{n+1}=u^{n+1}-u^n$, $\overline{V}=\Delta v^{n+1}=v^{n+1}-v^n$, $\overline{P}=\Delta p^{n+1}=p^{n+1}-p^n$ into Eqs. (4) and (5). Meanwhile, we draw the artificial compressibility factor β and pseudo-time τ into the equations as following:

$$\beta\frac{\partial\overline{P}}{\partial\tau}+\frac{\partial\overline{U}}{\partial x}+\frac{\partial\overline{V}}{\partial y}=0, \tag{6}$$

$$\frac{\partial \overline{U}}{\partial \tau}+\overline{U}+\frac{\Delta t}{2}\left\{\frac{\partial}{\partial x}\left[\overline{U}^2+2u^n\overline{U}+\overline{P}\right]+\frac{\partial}{\partial y}\left[\overline{UV}+v^n\overline{U}+u^n\overline{V}\right]-\frac{1}{Re}\left[\frac{\partial^2\overline{U}}{\partial x^2}+\frac{\partial^2\overline{U}}{\partial y^2}\right]\right\}$$
$$=-\Delta t\left\{\frac{\partial}{\partial x}\left[(u^n)^2+p^n\right]+\frac{\partial}{\partial y}(u^nv^n)-\frac{1}{Re}\left[\frac{\partial^2 u}{\partial x}+\frac{\partial^2 u}{\partial y}\right]^n\right\}=\text{R.H.}X. \tag{7}$$

$$\frac{\partial \overline{V}}{\partial \tau}+\overline{V}+\frac{\Delta t}{2}\left\{\frac{\partial}{\partial x}\left[\overline{UV}+v^n\overline{U}+u^n\overline{V}\right]+\frac{\partial}{\partial y}\left[\overline{V}^2+2v^n\overline{V}+\overline{P}\right]-\frac{1}{Re}\left[\frac{\partial^2\overline{V}}{\partial x^2}+\frac{\partial^2\overline{V}}{\partial y^2}\right]\right\}$$
$$=-\Delta t\left\{\frac{\partial}{\partial x}(u^nv^n)+\frac{\partial}{\partial y}\left[(v^n)^2+p^n\right]-\frac{1}{Re}\left[\frac{\partial^2 v}{\partial x}+\frac{\partial^2 v}{\partial y}\right]^n\right\}=\text{R.H.}Y. \tag{8}$$

Notice that there are two time-levels in this formulation, namely, physical time t and pseudo-time τ. Given a physical time step Δt , we can iterate the solution in pseudo-time τ until $\partial\overline{P}/\partial\tau$, $\partial\overline{U}/\partial\tau$ and $\partial\overline{V}/\partial\tau$ approach to zero. It is clear that once we get a convergent solution in the pseudo-time level, we get a transient-accurate solution in the physical time level simultaneously. To complete the formulation, the governing equations (6)–(8) are replaced by an implicit backward-difference approximation in pseudo-time τ. Non-linear numerical fluxes at the implicit pseudo-time level are linearized by Taylor expansion; then, spatial central-difference approximations are introduced. The result is a system of multidimensional, linear, couple difference equations for the dependent variables at the implicit pseudo-time level. To solve these equations, the approximate factorization or alternative direction implicit (ADI) scheme is used. The resulting system of equations can be written in narrow block-banded matrix structures and be solved efficiently by a standard LU decomposition method.

Using a fan to take the generated heat away from the electronic components, the dimensionless energy equation can be written as:

$$\frac{\partial T}{\partial t}+u\frac{\partial T}{\partial x}+v\frac{\partial T}{\partial y}=\kappa\left(\frac{\partial^2 T}{\partial x^2}+\frac{\partial^2 T}{\partial y^2}\right), \tag{9}$$

where $\kappa=1/(Re\times Pr)$, $Pr=\upsilon/\alpha$, Pr the Prandtl number, Re the Reynolds number, υ the kinematic viscosity and α is the thermal diffusivity. Eq. (9) is decoupled from the Navier–Stokes equations. Therefore, once the flowfield solution is obtained, the temperature distribution can be obtained by solving Eq. (9). In this study, we use backward time central space (BTCS) to discretize Eq. (9).

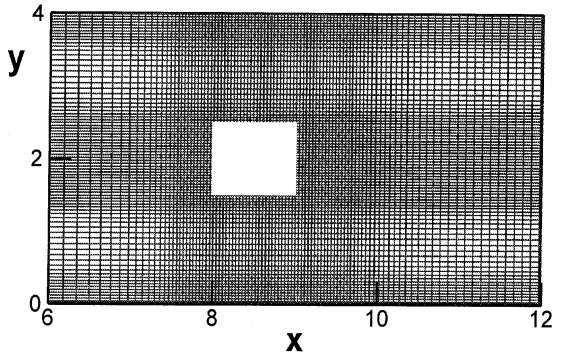

Fig. 1. The non-uniform grid of the channel.

The 2D coordinate system and non-uniform grid of the channel is depicted in Fig. 1, where L and W are the channel length and channel height, the $\Delta L=L_2-L_1$ and $\Delta W=W_2-W_1$ are the electronic components length and height. The boundary conditions that apply for Eqs. (6)–(9) are

2.1. Physical boundary conditions

Inflow

$$u_{\text{in}}=U_0,\quad v_{\text{in}}=0,\quad \left.\frac{\partial p}{\partial x}\right|_{\text{in}}=0,\quad T_{\text{in}}=T_\infty.$$

Outflow

$$\left.\frac{\partial u}{\partial x}\right|_{\text{exit}}=0,\quad \left.\frac{\partial v}{\partial x}\right|_{\text{exit}}=0,\quad p_{\text{exit}}=p_{\text{atm}},\quad \left.\frac{\partial T}{\partial x}\right|_{\text{exit}}=0.$$

Channel wall

$$u_{\text{wall}}=0,\quad v_{\text{wall}}=0,\quad \left.\frac{\partial p}{\partial y}\right|_{\text{wall}}=0,\quad \left.\frac{\partial T}{\partial y}\right|_{\text{wall}}=0.$$

Electronic component wall

$$u_{\text{wall}}=0,\quad v_{\text{wall}}=0,\quad \left.\frac{\partial p}{\partial n}\right|_{\text{wall}}=0,\quad T_{\text{wall}}=T_h.$$

2.2. Pseudo-time boundary conditions

Inflow

$$\overline{U}_{\text{in}}=0,\quad \overline{V}_{\text{in}}=0,\quad \left.\frac{\partial\overline{P}}{\partial x}\right|_{\text{in}}=0.$$

Outflow

$$\left.\frac{\partial\overline{U}}{\partial x}\right|_{\text{exit}}=0,\quad \left.\frac{\partial\overline{V}}{\partial x}\right|_{\text{exit}}=0,\quad \overline{P}_{\text{exit}}=0.$$

Channel wall

$$\overline{U}_{\text{wall}}=0,\quad \overline{V}_{\text{wall}}=0,\quad \left.\frac{\partial\overline{P}}{\partial y}\right|_{\text{wall}}=0.$$

Electronic component wall

$$\overline{U}_{\text{wall}} = 0, \quad \overline{V}_{\text{wall}} = 0, \quad \left.\frac{\partial \overline{P}}{\partial n}\right|_{\text{wall}} = 0,$$

where U_0, T_∞, T_h and P_{atm} are known constants.

3. Results and discussion

3.1. Verification of velocity field

In order to assure the accuracy of the computer program, the numerical results will now be presented for unsteady flows in a two-dimensional square cavity driven by the movement of the lid. First, we must set up certain conditions for cavity flow. The conditions are as follows:

1. The computational domain $(x, y) = (0\text{–}1, 0\text{–}1)$ is a 65×65 non-uniform grid.
2. The physical time is $\Delta t = 0.05$.
3. The pseudo-time $\Delta\tau$ will vary with the physical time. Generally, it is between 1 and 30 [9].
4. The artificial compressibility factor is generally between $1 \leqslant \beta \leqslant 100$ [9].
5. The initial condition of the pseudo-time is $\Delta\overline{P}^h = \Delta\overline{U}^h = \Delta\overline{V}^h = 0$.
6. The convergent condition of the pseudo-time is $\max(\Delta\overline{P}^{h+1}, \Delta\overline{U}^{h+1}, \Delta\overline{V}^{h+1}) \leqslant 10^{-5}$.

Here h is the iterative index of pseudo-time.

The streamline contours for the cavity flow configurations with $Re = 1000$ and $Re = 3200$ are shown in Fig. 2. A magnified view of the various secondary vortices is also included. The velocity components on the lines passing through the geometric center of the cavity (i.e., $x = 0.5$) are compared to the results of Ghia et al. [17] in Fig. 3. The origins of the plots have been shifted to the left for each successive Reynolds number case. The data of Ghia were obtained from a uniform grid of

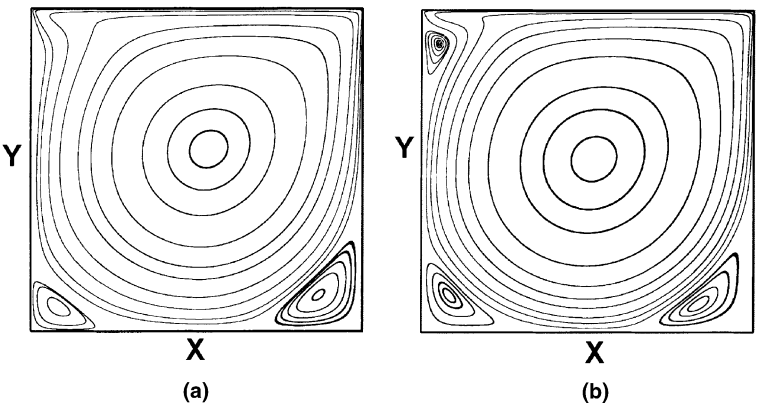

Fig. 2. Streamline contours for flow in driven cavity: (a) $Re = 1000$; (b) $Re = 3200$.

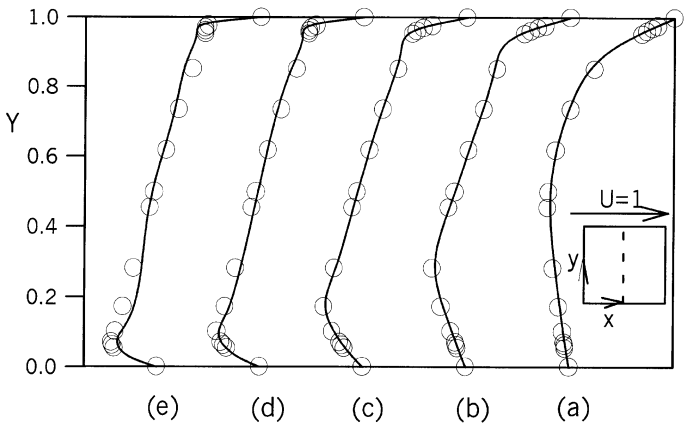

Fig. 3. The u-velocity profile with y at the center of cavity ($x = 0.5$) using a 65×65 non-uniform grid: (a) $Re = 100$; (b) $Re = 400$; (c) $Re = 1000$; (d) $Re = 3200$; (e) $Re = 5000$; ○ results obtained by 129×129 grid [17].

129×129 points for Reynolds numbers up to 3200, and a uniform grid of 257×257 points for Reynolds numbers 5000 and greater. It is seen that the present computed results agree very well with Ghia's solutions.

With regard to the transient-solution, Soh et al. [9] proposed that when the time approached zero, the drag coefficient C_D is defined to be a dimensionless drag force exerted on the lid, with

$$C_D = \frac{\text{drag force on the lid/length}}{\rho U_0^2 L} = \frac{D}{Re}, \tag{10}$$

where

$$D = \int_0^1 \left(\frac{\partial u}{\partial y}\right)_{y=1} \mathrm{d}x.$$

The theoretical drag coefficient on the lid can be shown to behave as

$$C_D = 0.035 t^{-1/2} \quad \text{for } t \to 0^+. \tag{11}$$

Fig. 4 plots the dimensionless drag force against $t^{-1/2}$, when $Re = 400$ and $\Delta t = 0.05$. In this figure, it is seen that the drag force yielded by the numerical method at a small time coincides with the theoretical drag coefficient. This proves that the present method yields the transient-accurate solution.

3.2. Verification of temperature field

To ensure the numerical accuracy of solving the energy equation, we continue using the cavity flow to verify the computer program. In the literature, Moallemi et al. [18] considered the flow and heat transfer in a square cavity where the flow is induced by a shear force resulting from the motion of the upper lid combined with the buoyancy force due to bottom heating. Tang et al. [19] solved the unsteady flow and studied the Grashof number effect on the temperature field. Chen et al. [20] studied the effects of the Reynolds number and Prandtl number (Pr) on the time-dependent flow field and temperature distribution in the cavity. We neglect the buoyancy effect and Richardson's numbers effect on the temperature field, because the buoyancy force and Richardson's numbers are very small in the present case. The boundary conditions are shown as in two different types in Fig. 5. We apply the boundary conditions and appoint $Pr = 1$, $Re = 1000$ to obtain the temperature field. Nusselt number is defined as

$$Nu = \frac{hl}{k} = \frac{\partial}{\partial(y/l)}\left(\frac{T_w - T}{T_w - T_\infty}\right)_w, \tag{12}$$

where h is convection coefficient, k thermal conductivity, T_w the temperature of wall and T_∞ is reference temperature. This equation is non-dimensionalized by the $\overline{T} = (T - T_w)/(T_\infty - T_w)$ and $\overline{y} = y/l$, the dimensionless

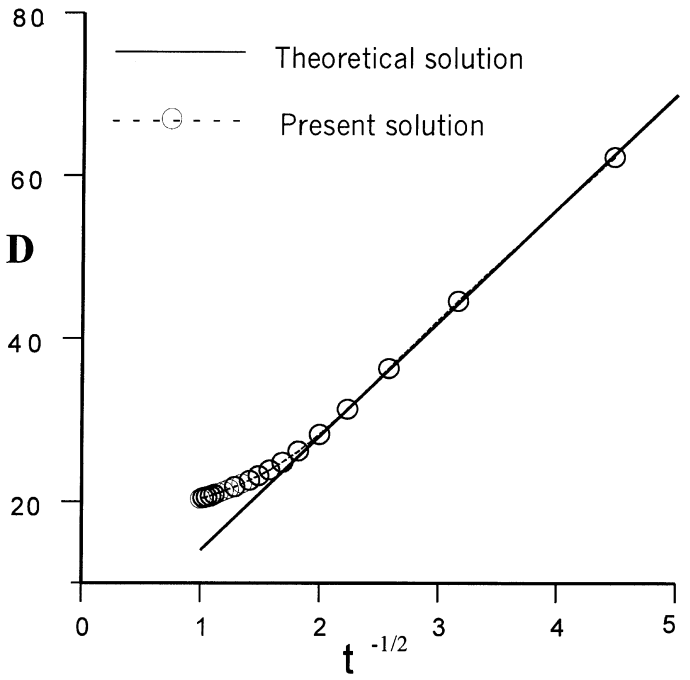

Fig. 4. Drag force D vs $t^{-1/2}$ using $\Delta t = 0.05$ when $Re = 400$.

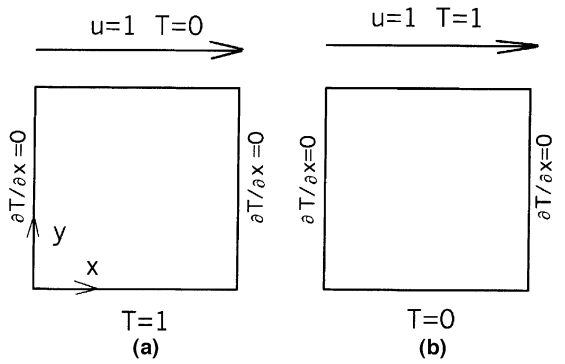

Fig. 5. The boundary conditions of the temperature field in the cavity.

form of Eq. (12) after dropping the head symbols can be written as:

$$Nu = -\left.\frac{\partial T}{\partial y}\right|_{w}. \tag{13}$$

In Fig. 6, the Nusselt numbers are plotted for the top lid and bottom plate and compared with solutions of Moallemi et al. [18] and Chen et al. [20], when $Re = 1000$. The data of Moallemi and Chen were obtained from a uniform grid of 41×41 points and 111×111 points, respectively. Our grids are non-uniform grids of 65×65 points. Fig. 6 clearly shows that the present solutions agree very well with Chen's result.

3.3. Analysis of flow though the electronic component

The fluid flow through a rectangular column will produce vortex shedding phenomenon, when the Reynolds number is larger than 50. In order to understand the effects of vortex shedding on both heat transfer and the flow field of the electronic components, using the previously described numerical method, computations have been carried out for flow around the electronic components for the Reynolds number between 100–1000. In the literature, Davis et al. [11,12] studied the cold flow over a rectangular cylinder without heat transfer. They found that the form of the upstream velocity profile ahead of the rectangle and the rectangular dimensions (length–width ratio) have important effect on the vortex shedding.

In Fig. 7, the velocity components (u and v) on the centerline just off the rear face of the electronic component are plotted against the time when $Re = 1000$. In this figure, it is seen that the velocity components behave like asymptotic periodic fluctuations. In general three quantities can be used to estimate the vortex shedding frequency: (1) the velocity components on the centerline just off the rear face of the electronic component; (2) the location of the stagnation point just off the front face of the electronic component; (3) the lift and drag coefficients. We used v-component to calculate the shedding frequency. The definition of Strouhal number is $St = fB/U_0$, where f is the shedding frequency, B the width of electronic component and U_0 is the reference velocity. The computed and experimental values of

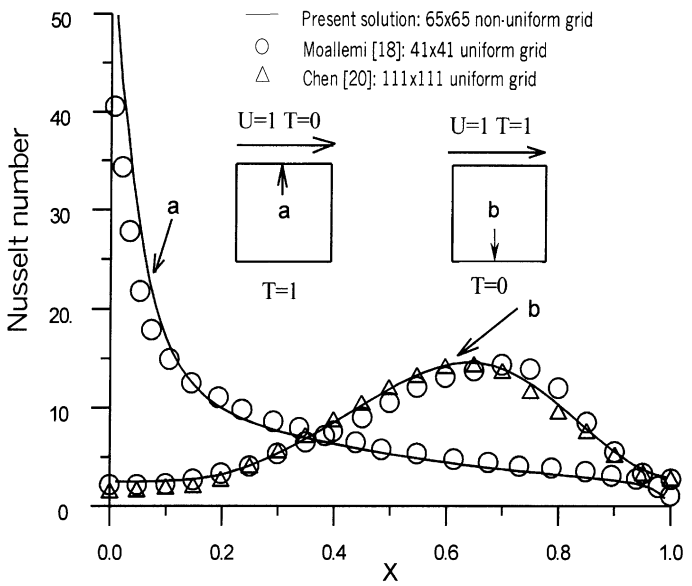

Fig. 6. Comparison of local Nusselt number over the cavity floor, and the lid with Moallemi and Jang [18] and Chen and Huang [20], when $Re = 1000$.

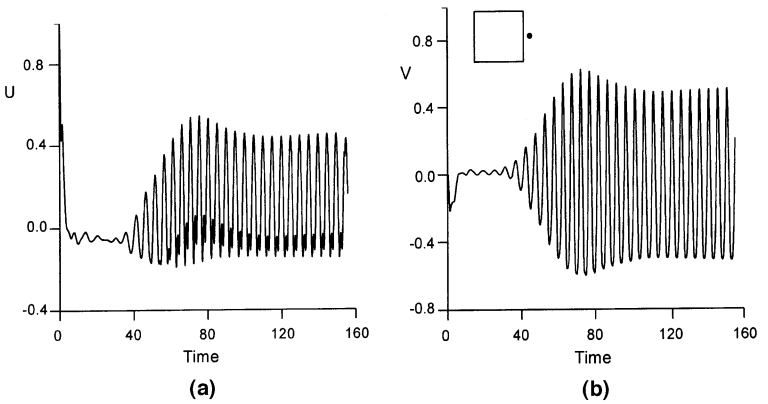

Fig. 7. The velocity components on the centerline just off the rear face of the electronic component are plotted against the time when $Re = 1000$.

Strouhal number are functions of Reynolds number as shown in Fig. 8. In this figure, our computed results are closer to the experimental data [12] than the [12] results of Davis et al. Notice that we used a non-uniform grid of 181×82 points. Davis used a non-uniform grid of 76×52 points.

To understand the unsteady flow physics, we first would like to see the large-scale flow structure. The large-scale flow structure can be obtained by $u' = u - \overline{u}$ to express the unsteady flow field, where u is an instantaneous velocity, and $\overline{u}$ is the average velocity. By using this method, it is possible to show the unsteady phenomenon of the flow clearly. Fig. 9 plots instantaneous velocity vectors in a cycle obtained from the large-scale flow structures when $Re = 250$. In this figure, the unsteady phenomenon caused by the vortex shedding, the size and the direction of the shear layer are clearly shown. In Fig. 9(a), there are five vortices being formed in this computational domain at 156.24 s. We denote them by the numbers from 1 to 5, respectively. The reduction of the vortex strength along the downstream with its serial number can be seen clearly. When the time is 157.59 s (see Fig. 9(b)), the vortex no. 6 is created, which is close to the rear surface of the

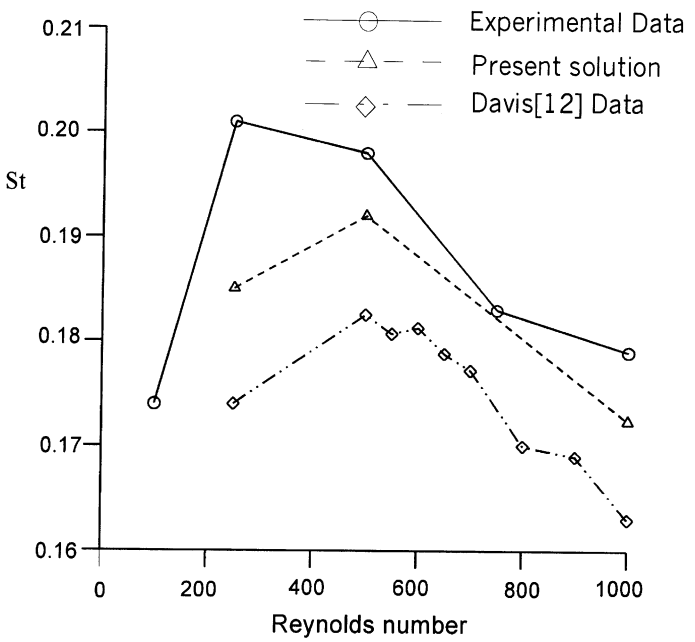

Fig. 8. Comparison of Strouhal number as a function of Reynolds number with Davis [12].

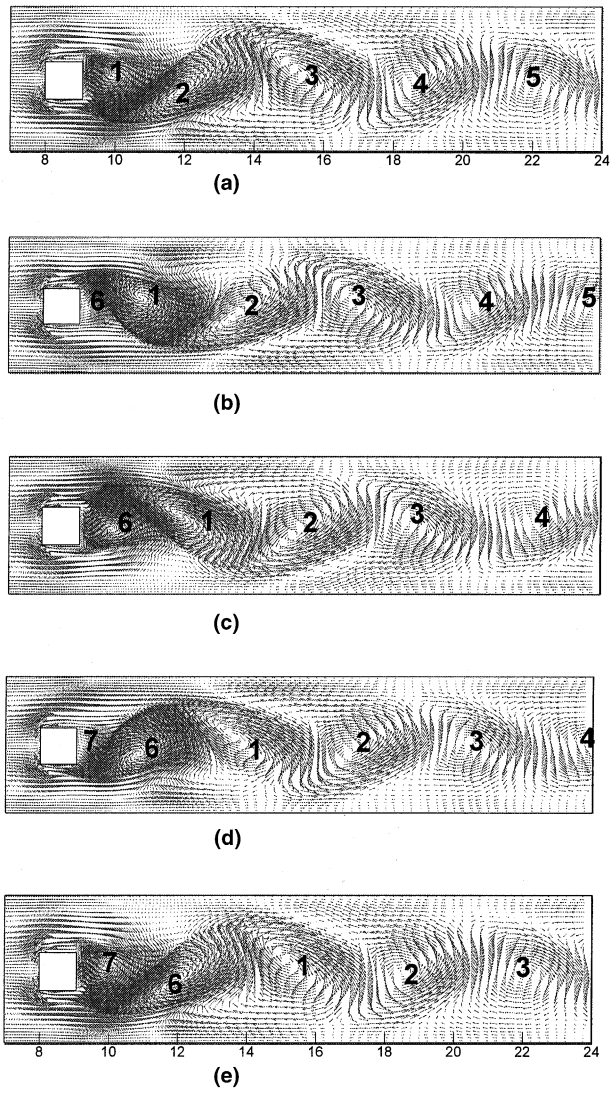

Fig. 9. The large-scale structure of the velocity vector at time: (a) 156.24; (b) 157.59; (c) 158.94; (d) 160.29; (e) 161.64 s, when $Re = 250$.

electronic component. At the same time, the vorticity of the shear layer makes the unsteady phenomenon even more obvious. Meanwhile, the five vortices (Nos. 1–5) are convecting to the downstream and their strengths are weakened due to viscous dissipation. At 160.29 s (see Fig. 9(d)), a new vortex No. 7 is being formed on the surface. At 161.64 s, the fluid structure returns to the structure where the time is 156.24 s, i.e., one cycle has been completed. In this cycle, we can clearly see the relationship between the formation of the vortex and its shedding, and the unsteady phenomenon of the flow field.

Next, we discuss the effect of vortex shedding on the surface pressure distributions of the electronic component. We define pressure coefficient as $C_p = 2\Delta P/\rho U^2$, where $\Delta P = P_{local} - P_{ref}$, P_{local} is the local pressure on the surface and P_{ref} is the referenced pressure. Fig. 10 plots the pressure coefficient distributions on the electronic component and the associated large-scale unsteady velocity vectors when $Re = 500$. In this figure, the pressure on the front of the electronic component is larger, because this surface is impacted directly by the fluid. The rear surface of the electronic component is adjacent to a counter-clockwise vortex. Therefore, the pressure on top of the rear surface is larger, because it is struck by the vortex. The bottom of the rear surface has smaller pressure because of the flow motion along the surface. We draw broken lines to represent typical streamline on the upper and lower sides of the surface. The flow between the surface and the streamline is

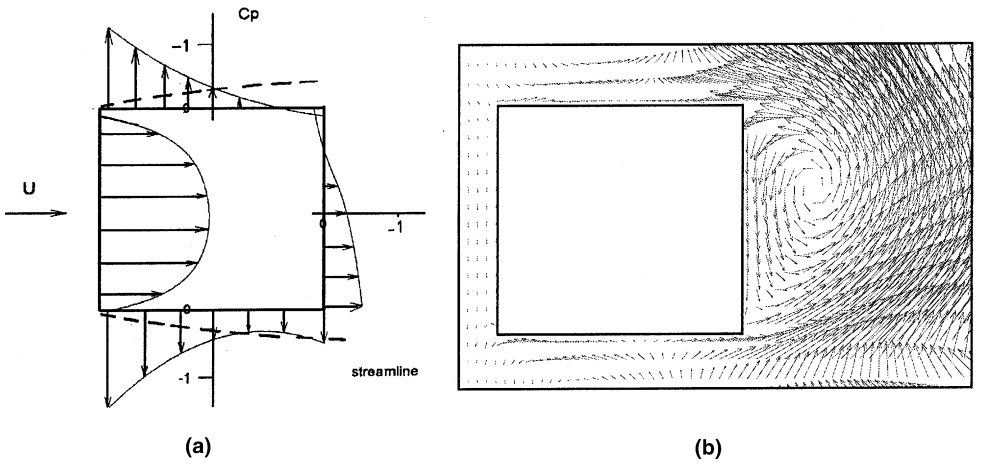

Fig. 10. The surface-pressure coefficient distribution and the large-scale structure of the velocity for electronic component at $Re = 500$.

similar to the flow through a diffuser. Therefore, the pressure at the leading edges is smaller than that at the trailing edges. Fig. 11 plots the pressure coefficient distributions and the large-scale unsteady velocity vectors when $Re = 1000$. In this figure, the vortex is slightly away from the rear surface of the electronic component. This results in smoother pressure distribution on the rear surface compared to the case with $Re = 500$.

The structure of the wake region downstream of the electronic component will now be discussed. It will be illustrated through the use of computed streakline and Davis's [12] experimental smoke–wire photographs. The flow visualizers here are passive marker particles introduced ahead of the body, a different symbol being used for each approaching streakline. In order to get the streakline, we used the Crank–Nicolson method to discretize the $dx/dt = U$. There are 20 streaklines with new particles being injected at time intervals of Δt. At time $t + \Delta t$ a given particle is moved a distance $\Delta t \times \boldsymbol{q}$ in the appropriate direction. The velocity $\boldsymbol{q}$ here is obtained by linear interpolation among the surrounding grid points. This is done at both time t and $t + \Delta t$ and then the two $\boldsymbol{q}s$ are averaged to obtain the particle velocity over the time span Δt. The particles are swept into the vortices behind the body and are shed with them, thus providing an excellent means for visualizing the motion of these large coherent structures as they move downstream away from the body. Figs. 12 and 13 present computed streakline plots and experimental [12] smoke–wire photographs showing the wake region downstream of the electronic component when $Re = 550$ and $Re = 100$, respectively. As can be seen here, the wake is

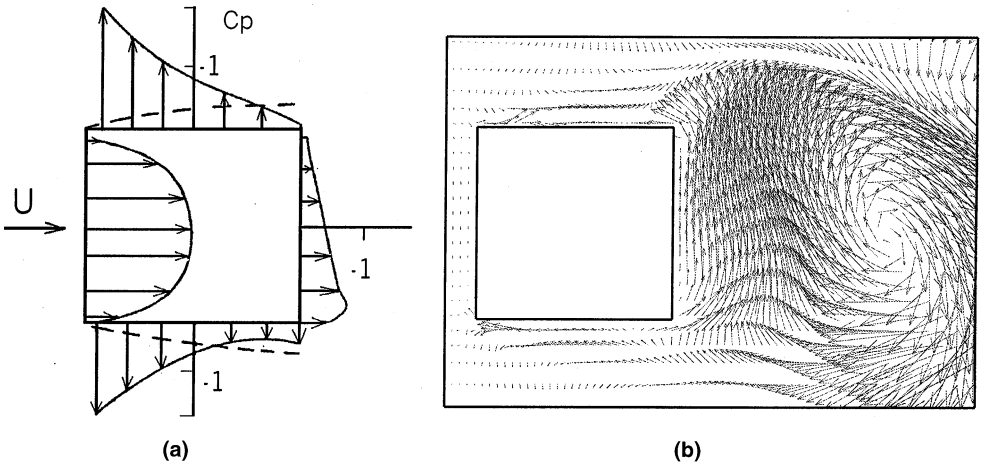

Fig. 11. The surface-pressure coefficient distribution and the large-scale structure of the velocity for electronic component at $Re = 1000$.

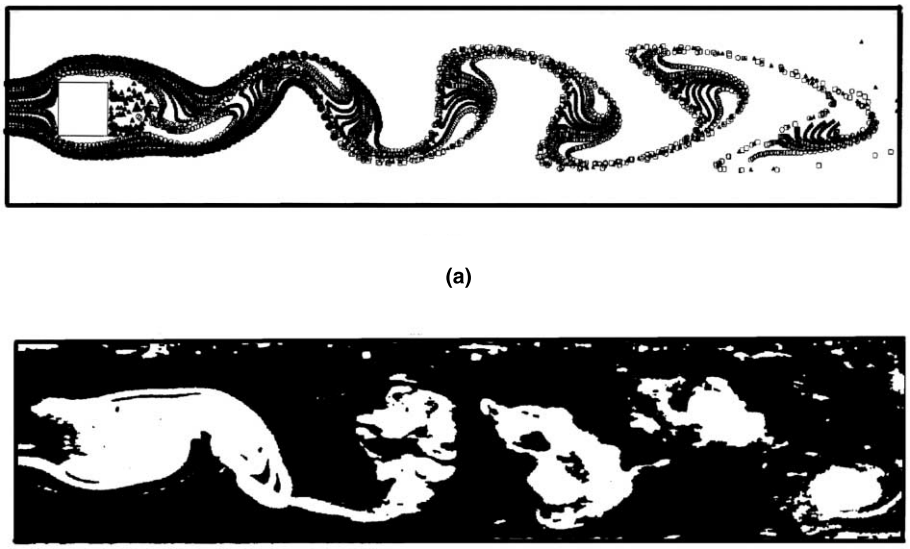

Fig. 12. Computed and Davis experimental [12] wake visualizations when $Re = 550$.

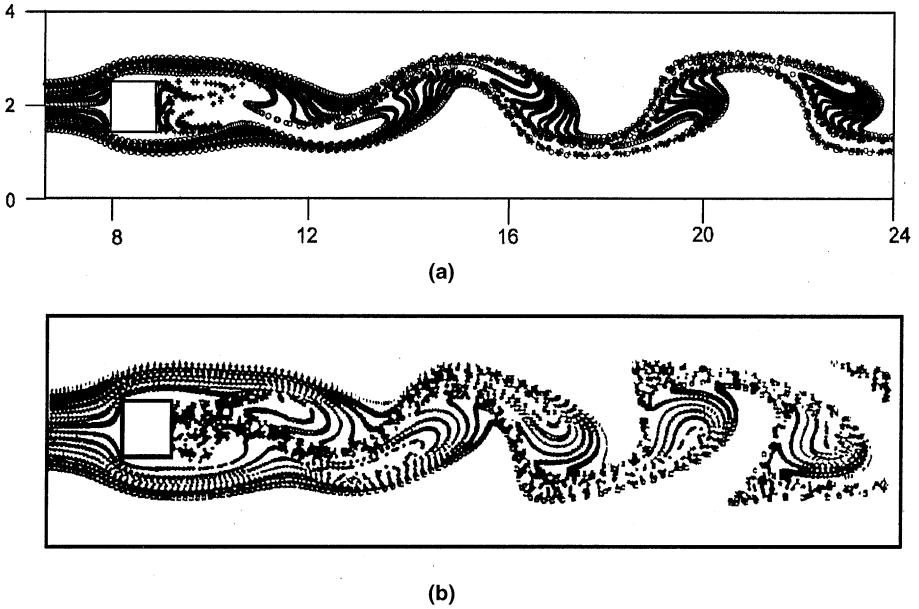

Fig. 13. Comparison of the streakline with Davis results [12] when $Re = 100$.

considerably more organized at the lower Reynolds number. The vortex cores in the experimental smoke–wire photograph in Fig. 12(b) appear to match well with those in the streakline plot in Fig. 12(a). The differences in the coherent structure between Figs. 12 and 13 are typical of the wake structure at low and high Reynolds numbers in the channel.

3.4. Analysis of the external thermal field of the electronic component

Before analyzing the thermal field, we have to judge whether the buoyancy force is important in the current problem. The Richardson number can be used to answer the question. The Richardson number is defined as

$$Ri = \frac{\text{buoyancy force}}{\text{inertial force}} = \frac{g\beta\Delta TL}{U^2} = \frac{Gr}{Re^2}, \quad (14)$$

where g is acceleration due to gravity, β the thermal expansion coefficient, L the reference length, Gr the Grash of number ($g\beta\Delta TL^3/\upsilon^2$), U the entrance velocity, Re the Reynolds number, and υ is the kinematic viscosity. For a typical example, when the length of electronic component is 6 mm, the working fluid is the air, the working temperature of the electronic components is kept at 70°C and the Reynolds number is 500. After calculation, the Richardson number is approximately 4.6×10^{-3}, which is very small compared to the inertial force. Therefore, the buoyancy effect is neglected in the momentum equations. Eq. (9) is decoupled to the Navier–Stokes equations. The equation can be solved numerically once the velocity field is obtained.

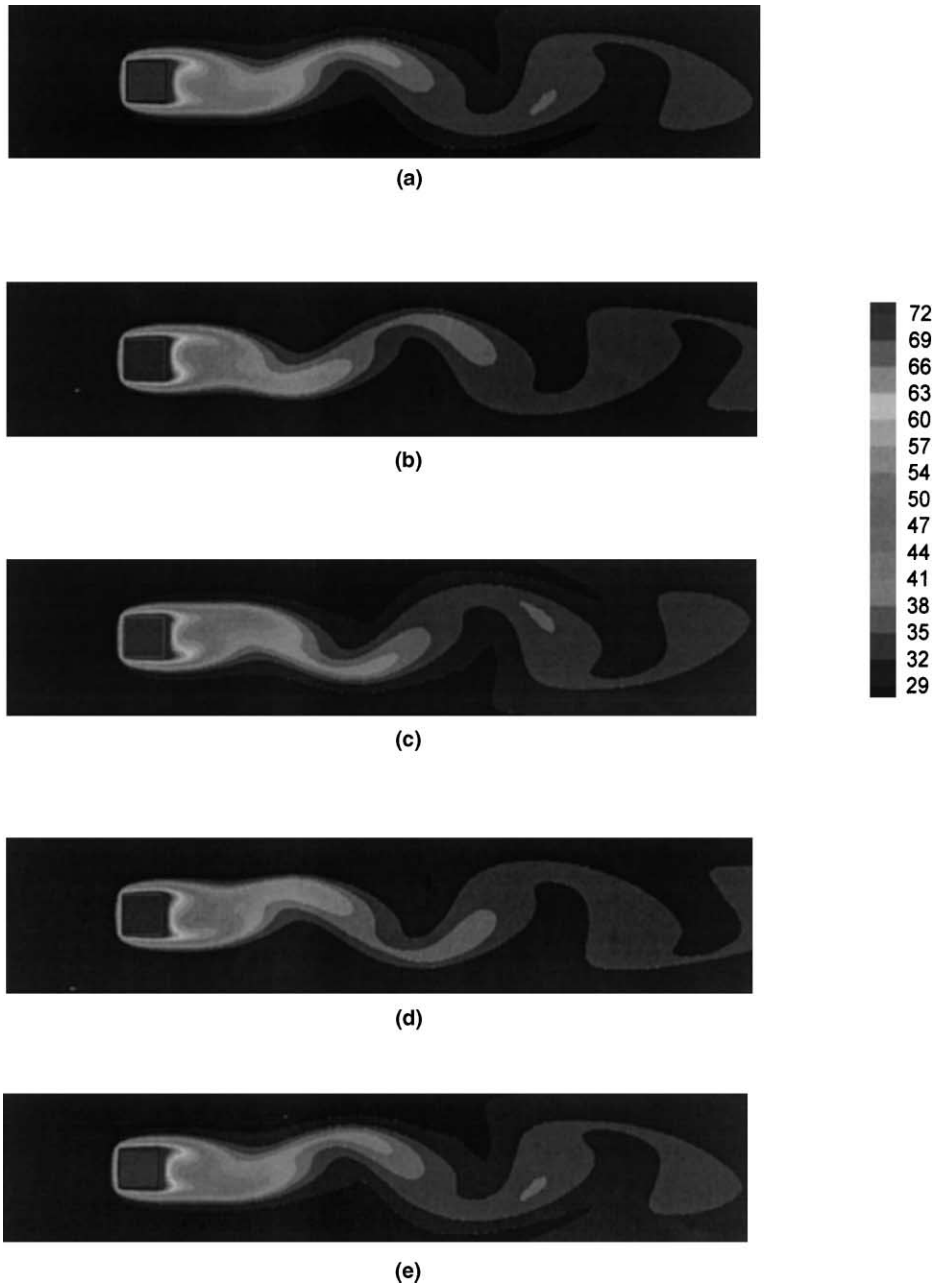

Fig. 14. The instantaneous temperature field at time: (a) 156.24; (b) 157.59; (c) 158.94; (d) 160.29; (e)161.64 s, when $Re = 250$.

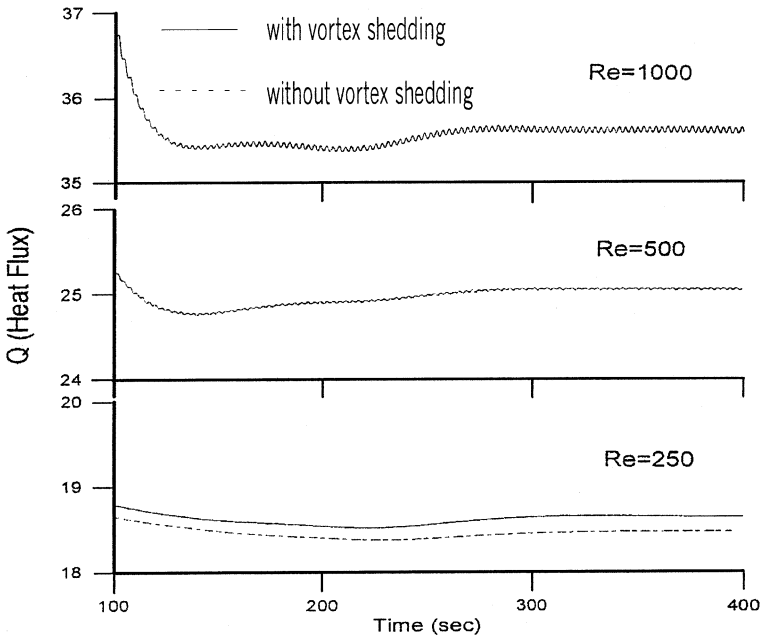

Fig. 15. The effect of Reynolds number on the surface heat transfer of the electronic component.

Fig. 14 shows five instantaneous temperature contours in a cycle when $Re = 250$. In this figure, it clearly shows how the thermal energy is being redistributed by the vortex shedding. The heat of the electronic component is taken away by the air to the downstream. This is important to keep the electronic component performing normally. In Fig. 15, the dimensionless total heat flux is plotted against the time for several Reynolds numbers. In order to understand whether the vortex shedding is helpful to the heat transfer, we also assume an ideal flow without the vortex shedding when $Re = 250$. In this figure, it is seen that the vortex shedding can enhance

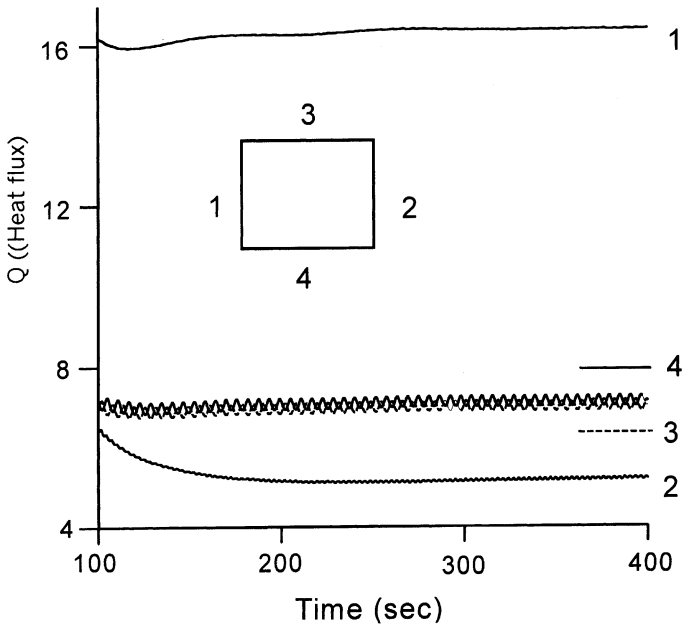

Fig. 16. The surface heat transfer of the electronic component when $Re = 1000$.

heat transfer compared to the ideal flow case when $Re = 250$. Also it shows that the larger Reynolds number results in larger heat flux.

Fig. 16 plots the heat flux distributions against the time for the four sides of the electronic component when $Re = 1000$. In this figure, the No. 1 side of the electronic component is directly impacted by the cooling fluid, therefore the heat transfer is largest. The No. 3 and 4 sides of the electronic component show oscillatory heat flux, and the curves are complementary. They are caused by the vortex shedding. The No. 2 side of the electronic component has a smaller heat flux, due to the thermal energy being trapped in the vortex next to the rear surface.

Figs. 17 and 18 plot the surface heat transfer distribution of the electronic component and the associated large-scale flow structure when $Re = 500$ and $Re = 1000$. In those figures, the surface a has larger heat transfer compared to other surfaces, because it is directly impacted by the cooling fluid. The heat transfer of the surface c and d decreases along the flow direction, due to the heat flux in the upstream is convected to the downstream by the fluid. In Fig. 17, there is a counter-clockwise vortex in the rear part next to the surface b of the electronic component. The vortex sucks the cooling air from the lower side to the upper side. Therefore, both top and bottom parts of the surface b have larger heat transfer compared to the middle portion of the surface. In Fig. 18, the heat transfer of the rear side (surface b) is similar to that in Fig. 17, but the vortex is in clockwise direction.

The temperature contour and the computed streakline for $Re = 250$ are depicted in Fig. 19. It can be seen that the temperature contour and the computed streakline are very similar. This is because the temperature is only a passive scalar in the present model.

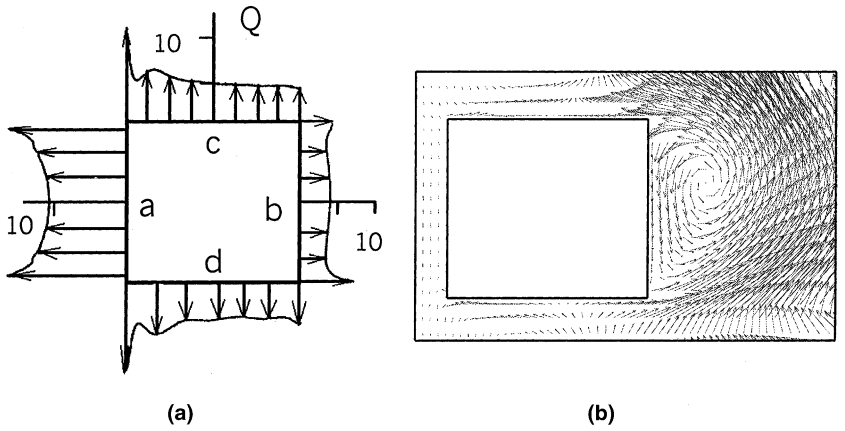

Fig. 17. The surface heat transfer distribution and the large-scale flow structure for electronic component at $Re = 500$.

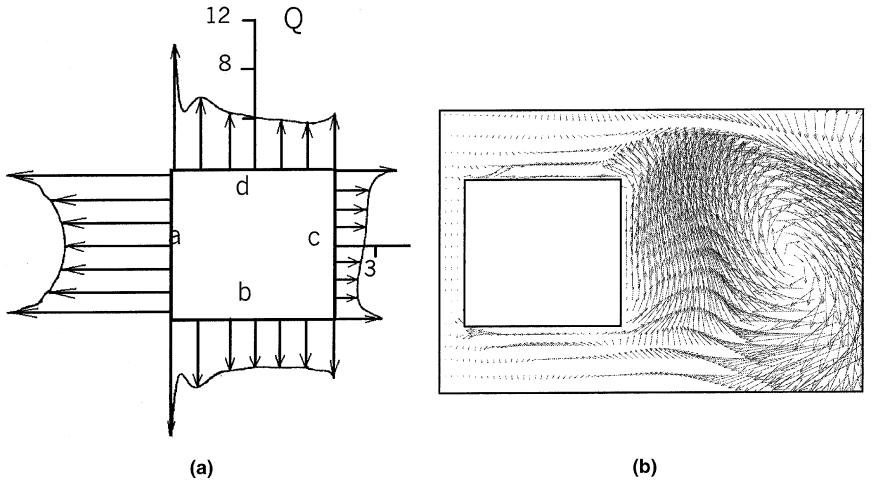

Fig. 18. The surface heat transfer distribution and the large-scale flow structure for electronic component at $Re = 1000$.

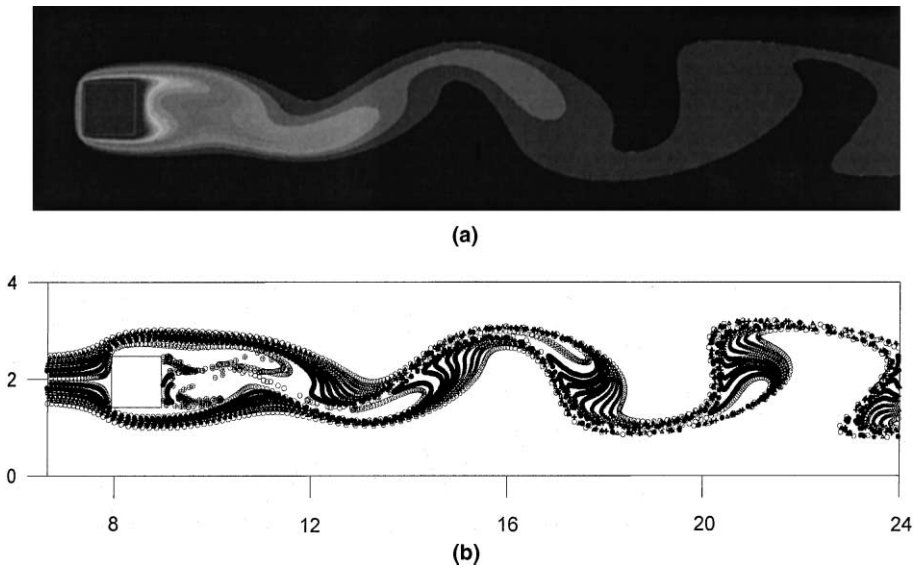

Fig. 19. Comparison of the computed temperature field and the streakline when $Re = 100$.

Therefore, we can regard the temperature distribution as the streakline structure.

4. Conclusion

In this study, we use dual-time steps approach to improve the artificial-compressibility method in order to obtain transient-accurate solution. The method has been verified by testing several benchmark problems. The proposed model is applied to study the unsteady heat transfer of a flow past a heated electronic component. The large-scale flow structure, vortex shedding and heat transfer are discussed.

The following conclusions can be drawn:

1. The computed Strouhal number for the flow past the heated electronic component is very close to Davis's experiment data [11,12].
2. We use the large-scale flow structure to study the vortex shedding mechanism. The structure reveals the unsteady phenomenon caused by the vortex shedding. Also, we can understand the shear layer phenomenon between two vortices. The vortex gradually decreases its strength along the downstream.
3. We obtain the streakline by using the relationship between the position and the time deviation, and it matches well with those in Davis's experiment.
4. From the computed results of the pressure coefficient, the pressure on the front side is larger than the other sides, because it is impacted directly by the fluid. In other words, the pressure is mainly generated by the direct impact on the front side of the electronic component.
5. From the computed results of the heat transfer on the electronic component surface, the heat flux of the rear side on the electronic component is much less than other sides, due to the trapping of energy in the vortex next to the rear surface. The heat flux for the case of flow with vortex shedding is higher than that without vortex shedding.
6. The temperature is a passive scalar in the present model. We can use the temperature field as the structure of the streakline.

This study provides detail flow structure and heat transfer mechanism which may serve fundamental knowledge in designing electronic cooling. Further study is also required to consider internal heat generation of the electronic component and its conjugate heat transfer with external flow as well as 3D effects.

References

[1] A.J. Chorin, A numerical method for solving incompressible viscous flow problems, J. Comput. Phys. 2 (1967) 12–26.
[2] D. Kawk, J.L.C. Chang, S.P. Shanks, S.R. Chakravarthy, A three-dimensional incompressible Navier–Stokes flow solver using primitive variables, AIAA J. 24 (3) (1986) 390–396.
[3] J.L.C. Chang, D. Kwak, S.E. Rogers, R.-J. Yang, Numerical simulation methods of incompressible flows and an application to the space shuttle main enging, Int. J. Numer. Methods Fluids 8 (1988) 1241–1268.
[4] W.Y. Soh, Time-marching solution of incompressible Navier–Stokes equation for internal flow, J. Comput. Phys. 70 (1987) 232–252.
[5] J.D. Ramshaw, V.A. Mousseau, Accelerated artificial compressibility method for steady-state incompressible flow calculations, Comput. Fluids 18 (4) (1990) 361–367.

[6] R.-J. Yang, J.L.C. Chang, D. Kwak, Navier–Stokes flow simulation of the space shuttle main engine hot gas manifold, AIAA J. Spacecraft Rocket 29 (2) (1992) 253–259.
[7] S.E. Rogers, D. Kwak, An upwind difference scheme for the incompressible Navier–Stokes equations, Appl. Numer. Math. 8 (1991) 43–46.
[8] S.E. Rogers, D. Kwak, C. Kiris, Steady and unsteady solutions of the incompressible Navier–Stokes equations, AIAA J. 29 (1988) 603–610.
[9] W.Y. Soh, J.W. Goodrich, Unsteady solution of incompressible Navier–Stokes equations, J. Comput. Phys. 79 (1988) 113–134.
[10] R.-J. Yang, Y.-R. Jeng, L.-M. Fu, A study on eliminating factorization and linearization errors, Comput. Fluid Dynamics J. 7 (4) (1999) 397–404.
[11] R.W. Davis, E.F. Moore, A numerical study of vortex shedding from rectangles, J. Fluid Mech. 116 (1982) 475–506.
[12] R.W. Davis, E.F. Moore, L.P. Purtell, A numerical experimental study of confined flow around rectangular cylinders, Phys. Fluids 27 (1984) 46–59.
[13] J.E. Fromm, F.H. Harlow, Numerical solution of vortex street development, Phys. Fluids 6 (1963) 975–983.
[14] K. Azar, E.T. Russell, Effect of component layout and geometry on the flow distribution in electronics circuit packs, J. Electronic Packaging 113 (1991) 50–57.
[15] A. Zebib, Y.K. Wo, A two-dimensional conjugate heat transfer model for forced air cooling of an electronic device, J. Electronic Packaging 111 (1989) 41–45.
[16] S.Y. Kim, H.J. Sung, J.M. Hyun, Mixed convection from multiple-layered boards with cross-streamwise periodic boundary conditions, Int. J. Heat Mass Transfer 35 (11) (1992) 2941–2952.
[17] U. Ghia, K.N. Ghia, C.T. Shin, High-Re Solution for incompressible flow using the Navier-Stokes equations and a multigrid method, J. Comput. Phys. 48 (1982) 387–411.
[18] M.K. Moallemi, K.S. Jang, Prandtl number effects on laminar mixed convection heat transfer in a lid-driven cavity, Int. J. Heat Mass Transfer 35 (8) (1992) 1881–1892.
[19] L.Q. Tang, T.H. Tsang, Transient solution by a least-squares finite-element method and jacobi conjugate gradient technique, Numer. Heat Transfer, Part B 28 (1995) 183–198.
[20] P.H. Chen, K.C. Huang, Convective transport phenomena in an impulsively started lid-driven open-cavity flow, Numer. Heat Transfer, Part A 29 (1996) 511–524.